Supporting Information

Cooperative Assembly of Magneto-nanovesicles with Tunable Wall Thickness and Permeability for MRI-guided Drug Delivery

Kuikun Yang,[†,#] Yijing Liu,[†,‡,#] Yi Liu,[†] Qian Zhang,[†] Chuncai Kong,[†] Chenglin Yi,[†] Zijian Zhou,[‡] Zhantong Wang,[‡] Guofeng Zhang,[‡] Yang Zhang,[§] Niveen M. Khashab,[§,] Xiaoyuan Chen,[‡,*] and Zhihong Nie[†,*]*

[†] Department of Chemistry and Biochemistry, University of Maryland College Park, Maryland 20742 (USA)

[‡] Laboratory of Molecular Imaging and Nanomedicine (LOMIN), National Institute of Biomedical Imaging and Bioengineering (NIBIB), National Institutes of Health, Maryland 20892 (USA)

[§] Smart Hybrid Materials (SHMs) Lab, Department of Chemical Sciences and Engineering, Advanced Membranes and Porous Materials Center, King Abdullah University of Science and Technology (KAUST), Thuwal 23955-6900 (Kingdom of Saudi Arabia)

Corresponding author E-mails: znie@umd.edu, shawn.chen@nih.gov, niveen.khashab@kaust.edu.sa

[#]These authors contributed equally.

Synthesis of maleimide-terminated dopamine

Maleimide-terminated dopamine was synthesized by the carbodiimide reaction following a previously reported procedure.[1] Briefly, Dopamine hydrochloride (1.92 g, 0.010 mol) and triethylamine (1.28 g, 0.013 mol) were dissolved in anhydrous methanol (10 ml) and then added dropwise to a solution of 6-maleimidohexanoic acid N-hydroxysuccinimide ester (2.6 g, 0.008 mol) in anhydrous CH_2Cl_2 (100 ml). The mixture was stirred vigorously for 48 h under nitrogen and washed three times with HCl (0.5M, 80 ml). The solvent was evaporated and the crude product was purified by column chromatography (SiO_2/CH_2Cl_2/MeOH 10:1).

Supplementary Figures

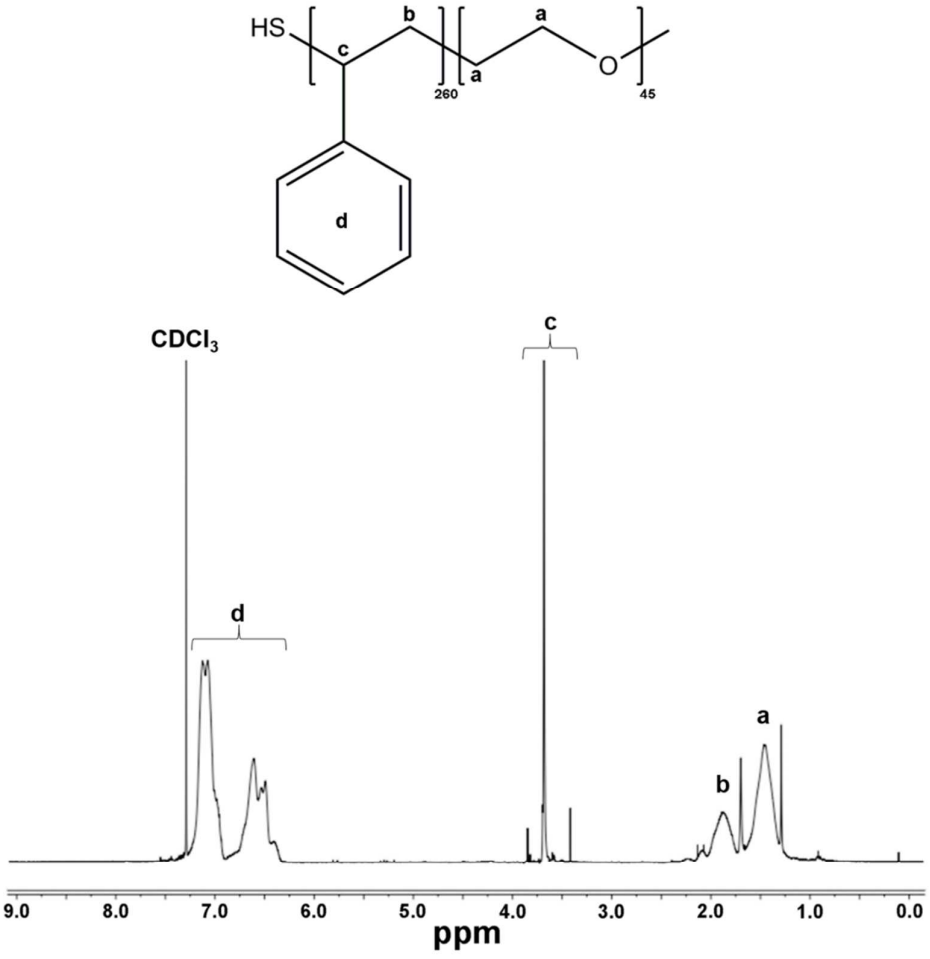

Figure S1. ^{1}H NMR spectrum of PEO-*b*-PS.

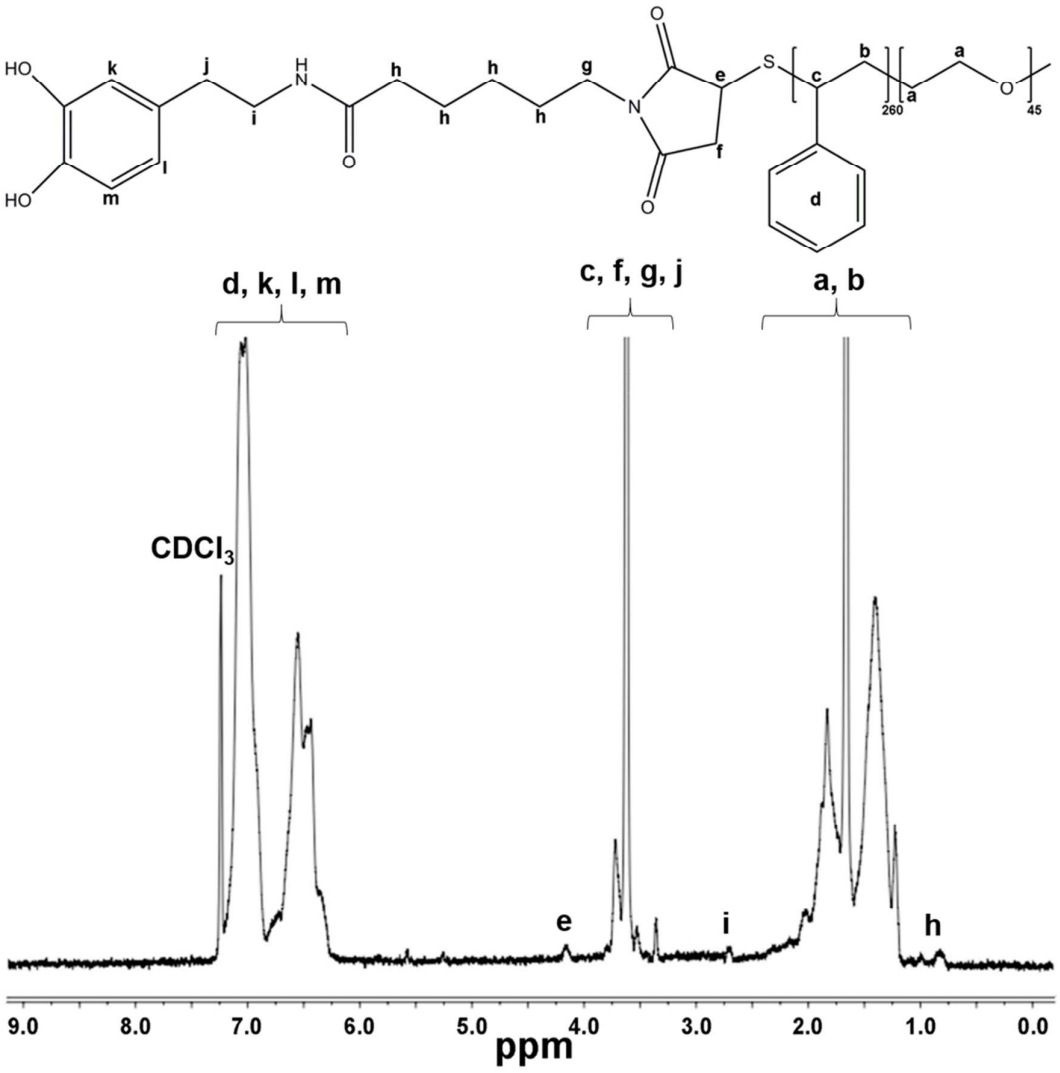

Figure S2. ^{1}H NMR spectrum of dopamine-terminated PEO-*b*-PS.

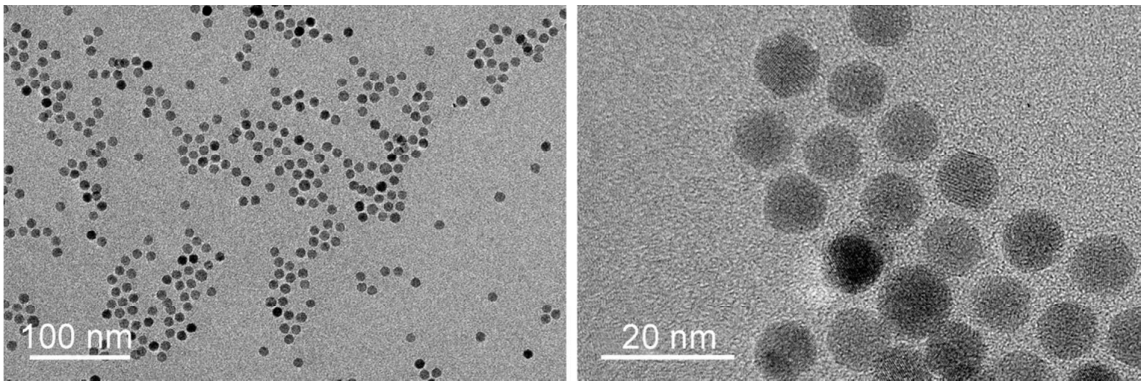

Figure S3. TEM images of SPIONs before the self-assembly.

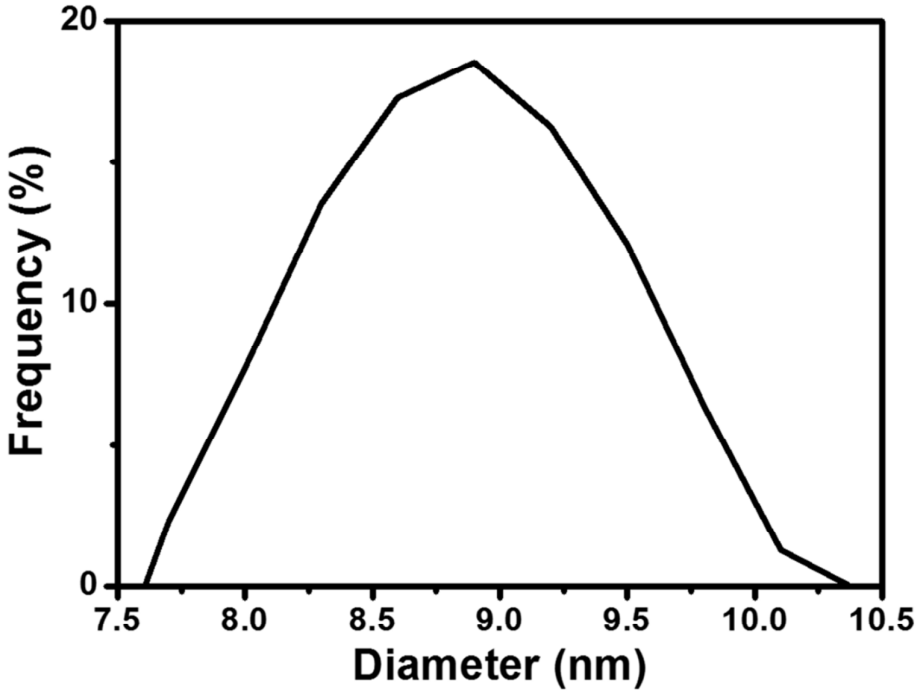

Figure S4. Size distribution of SPIONs from TEM analysis.

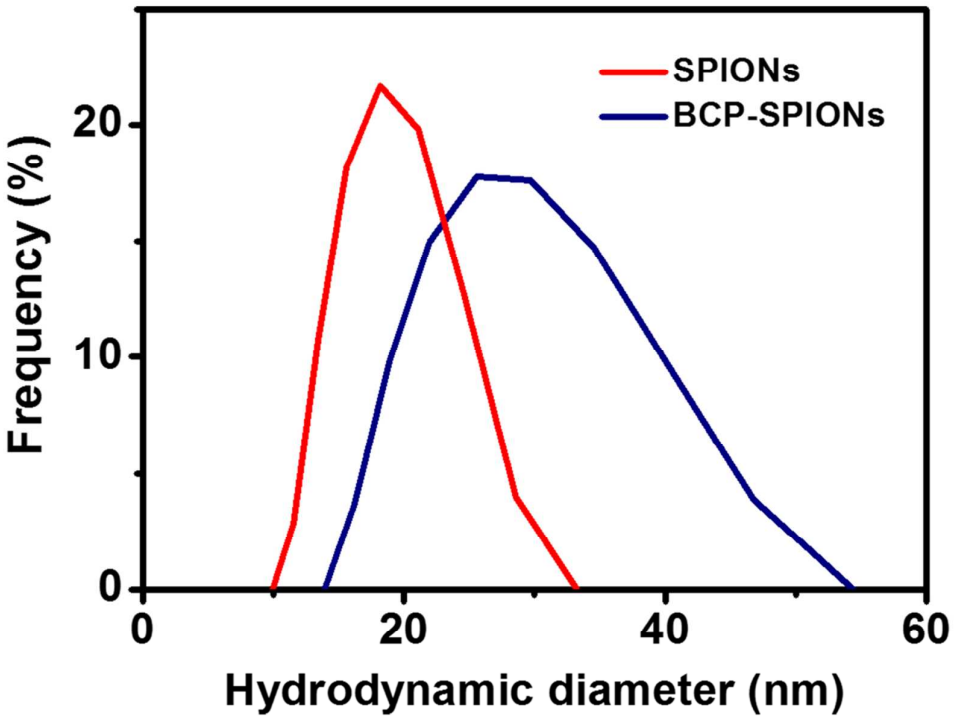

Figure S5. Dynamic light scattering analysis of the hydrodynamic diameter of SPIONs in THF before (red) and after (blue) the grafting of amphiphilic PEO-*b*-PS on the surface.

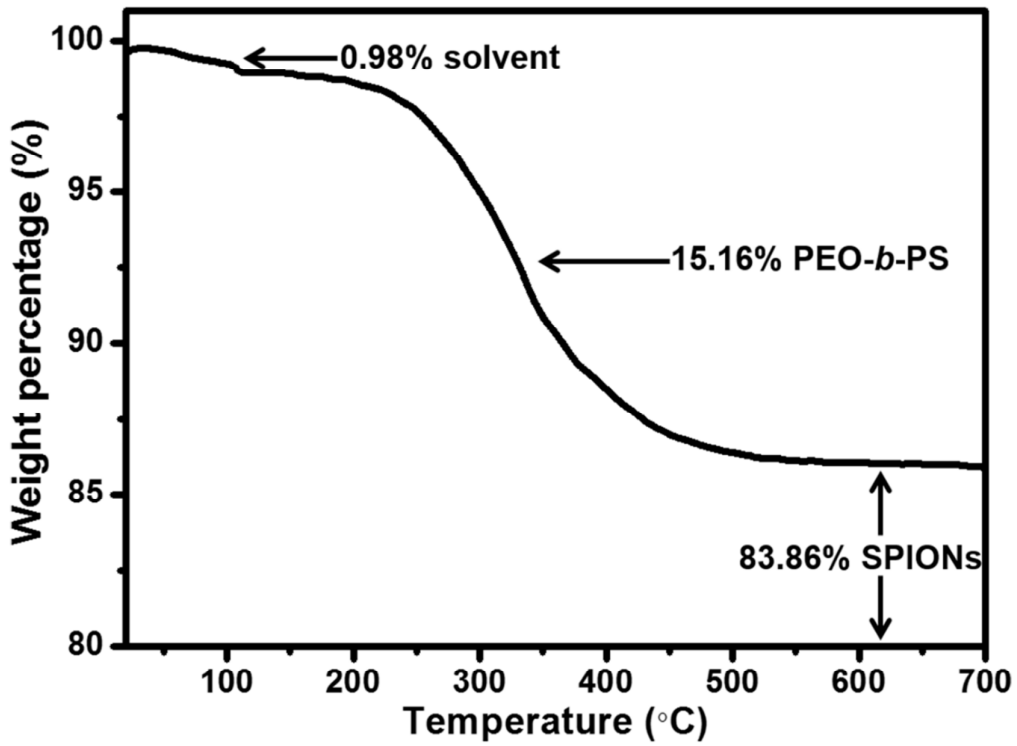

Figure S6. TGA results of PEO-*b*-PS-tethered SPIONs.

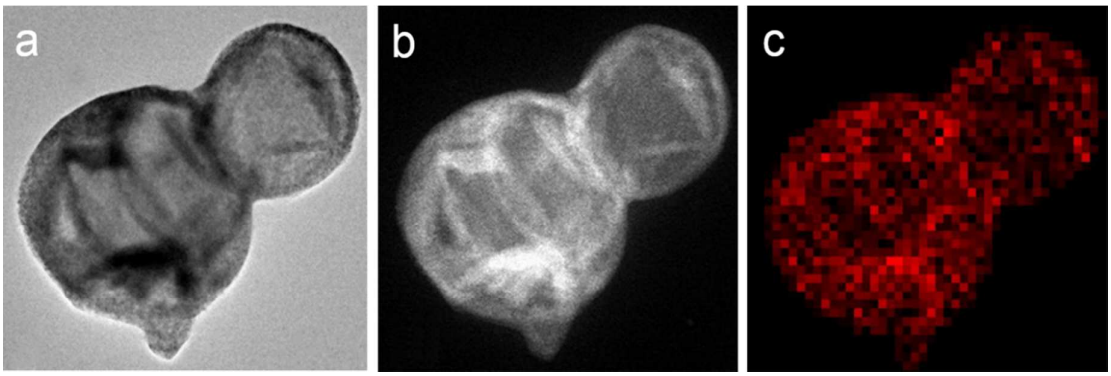

Figure S7. (a,b) STEM images and (c) the corresponding EDS element mapping (Fe) image of MuMVs.

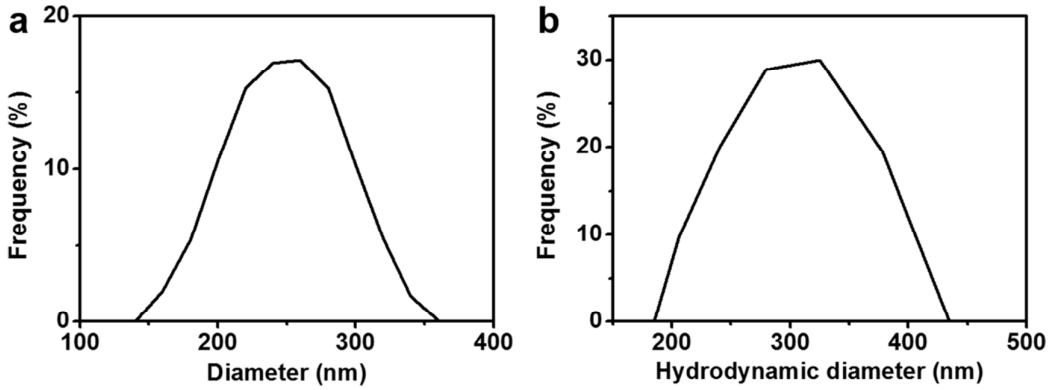

Figure S8. (a) TEM analysis of the diameter of MuMVs dried on TEM grid and (b) dynamic light scattering measurement of the diameter of MuMVs dispersed in water.

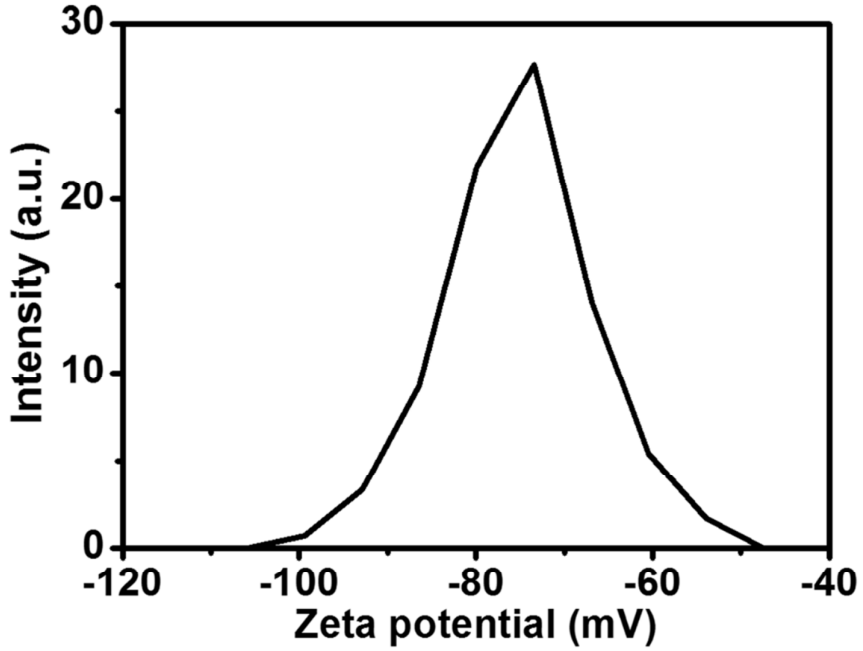

Figure S9. Zeta potential measurement of MuMVs indicates that the MuMVs are negatively charged due to the presence of carboxyl groups in PS-*b*-PAA.

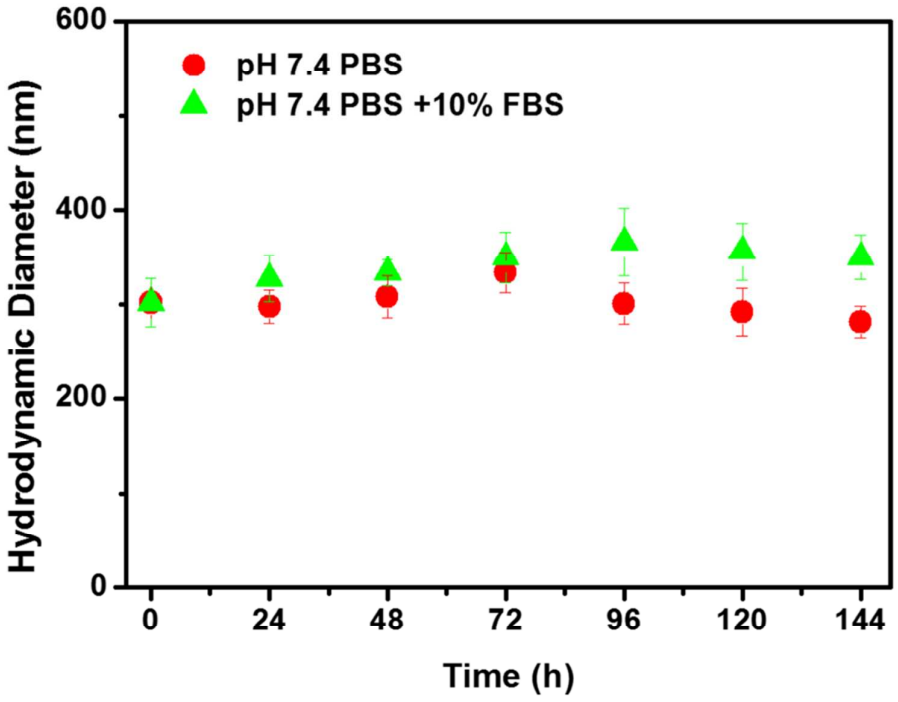

Figure S10. Hydrodynamic size distribution of MuMVs in PBS and PBS supplemented with 10% FBS

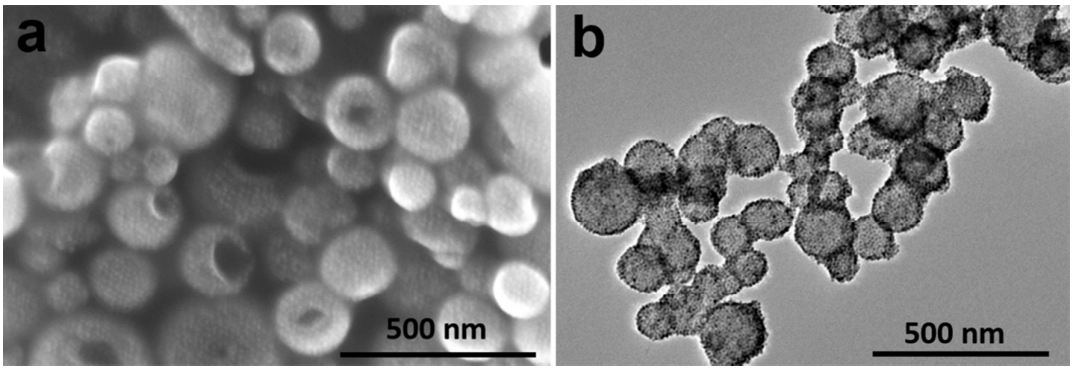

Figure S11. (a) SEM and (b) TEM images of MoMVs. The occasional buckling and collapse of the membrane indicates the formation of hollow vesicular structures

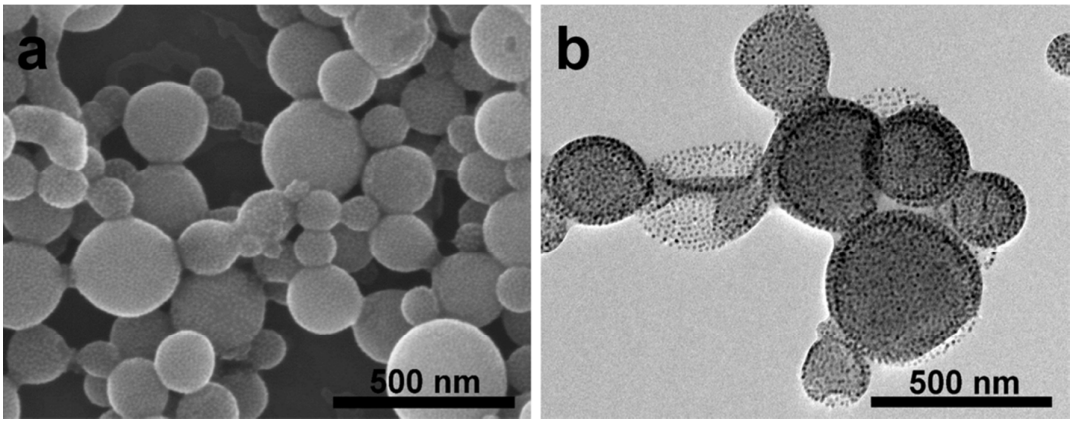

Figure S12. (a) SEM and (b) TEM images of DoMVs. The wrinkling and buckling of the membrane indicates the formation of hollow vesicular structures.

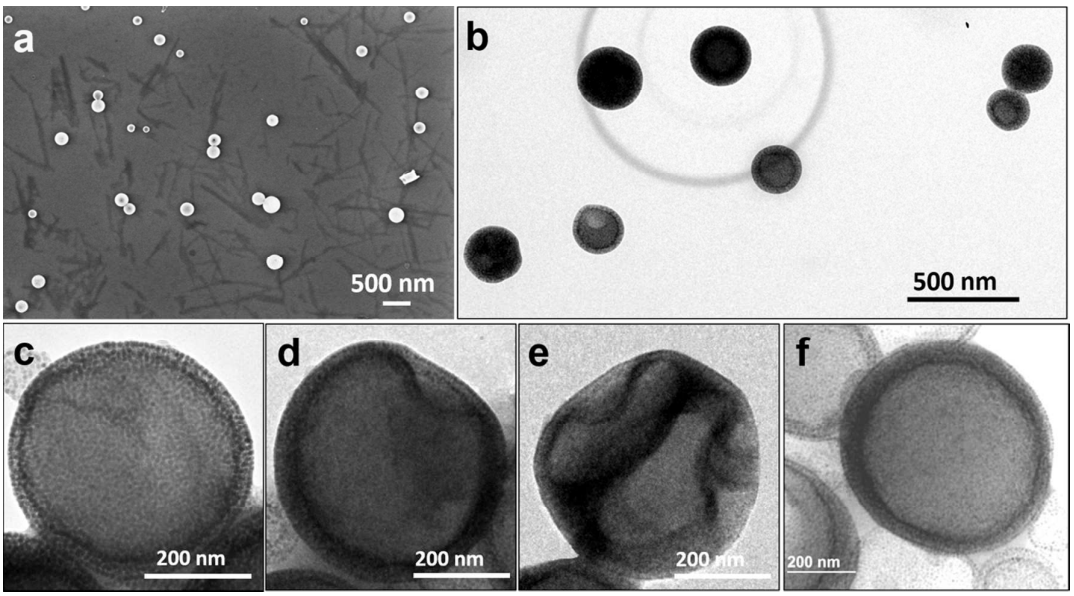

Figure S13. (a) SEM and (b-f) TEM images of MuMVs. The wrinkling and buckling of the membrane further indicates the formation of hollow vesicular structures.

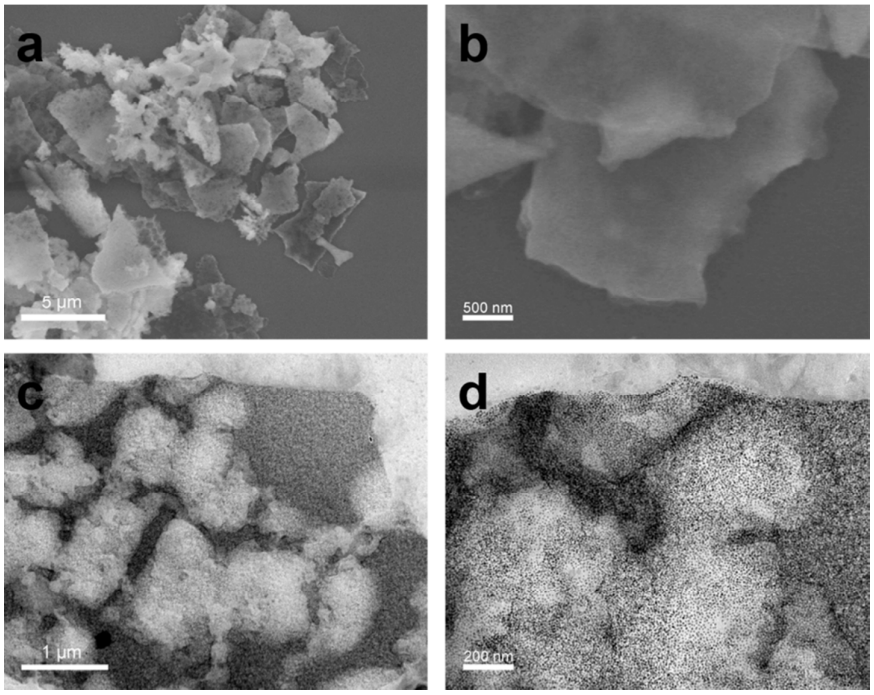

Figure S14. Representative (a,b) SEM and (c,d) TEM images of magnetic aggregates.

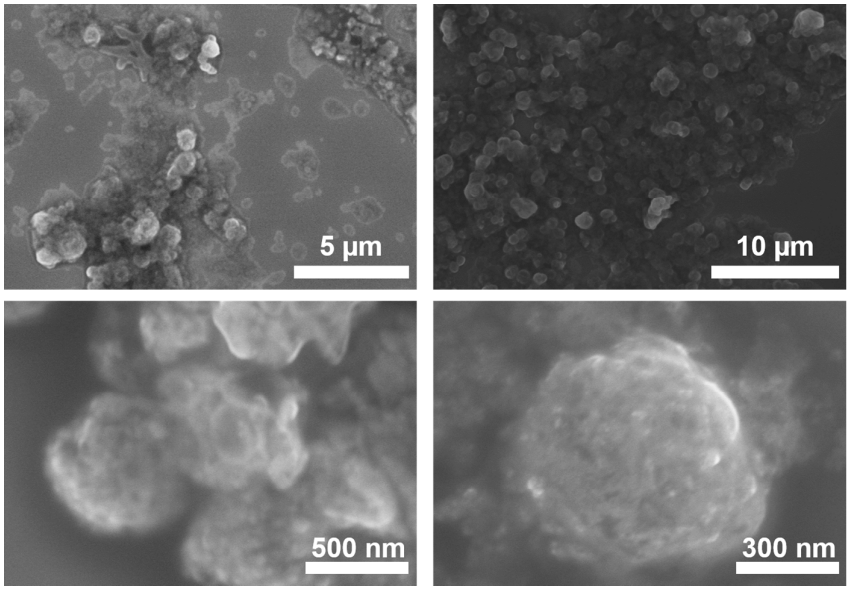

Figure S15. Representative SEM images of irregular aggregates assembled from a mixture of PS-b-PEO grafted SPIONs and free PS-b-PEO. When PS-b-PAA was replaced by PS-b-PEO without affinity to the surface of SPIONs, the assembly did not produce MVs with tunable layers of SPIONs in the membranes.

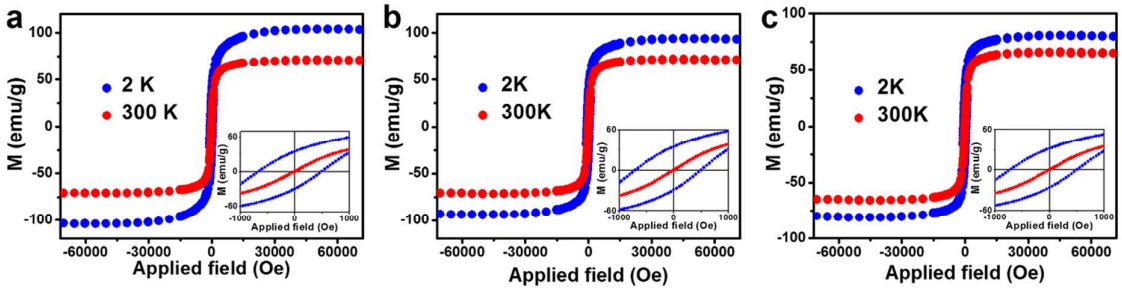

Figure S16. Hysteresis curves of (a) SPIONs (b) MoMVs and (c) DoMVs measured at 300 and 2 K.

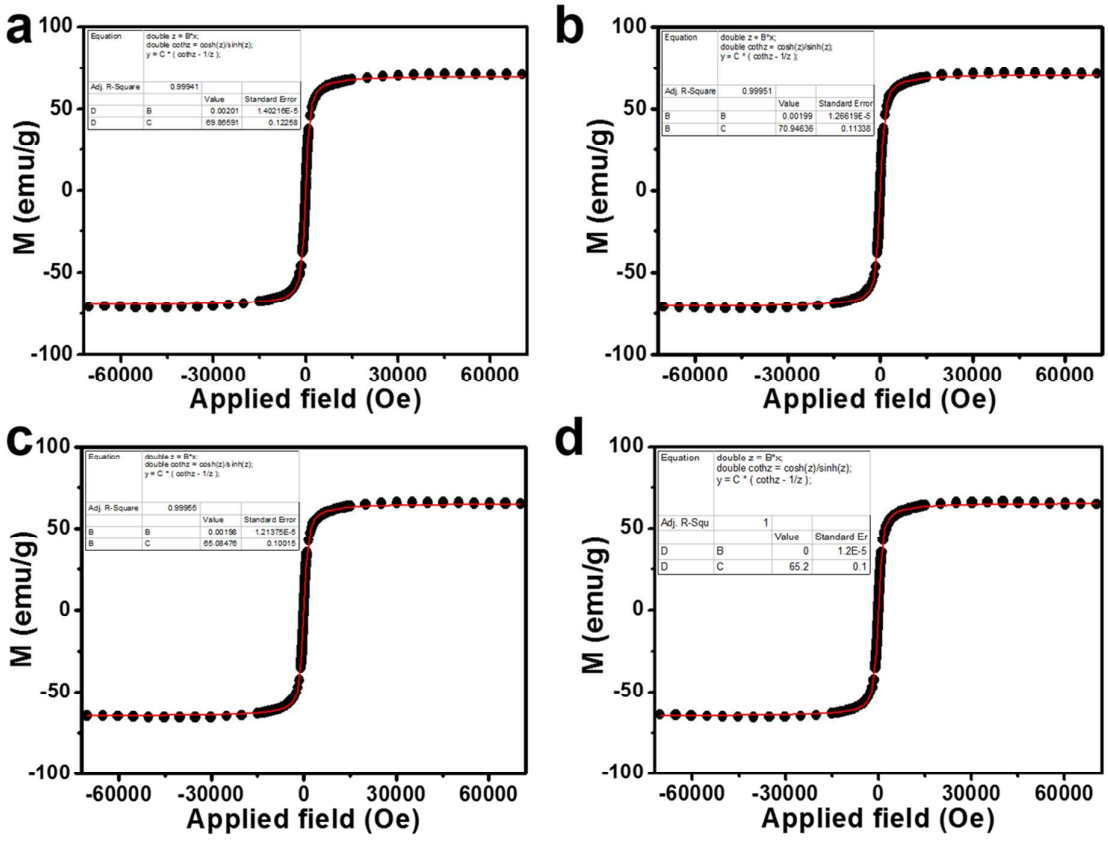

Figure S17. The magnetization of (a) individual SPIONs, (b) SPIONs in MoMVs, (c) SPIONs in DoMVs and (d) SPIONs in MuMVs was obtained by fitting the data into the Langevin paramagnetic function.

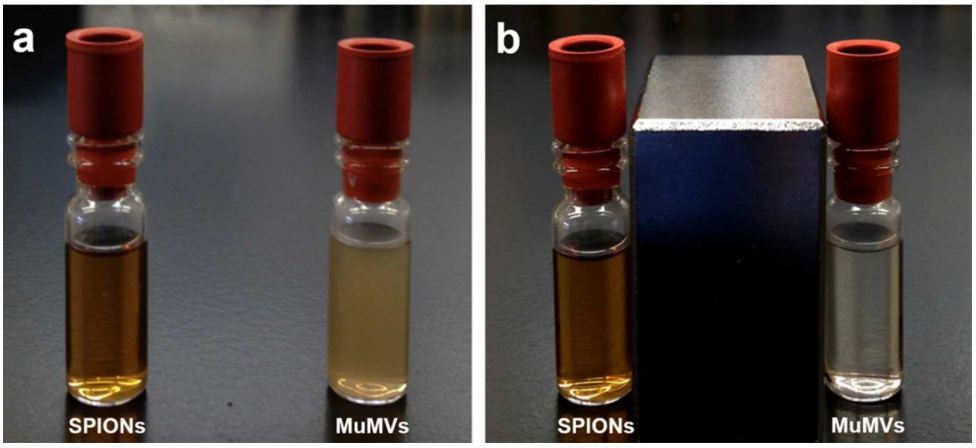

Figure S18. Photographs of equal concentrations of aqueous SPIONs and MuMVs dispersions (a) without magnetic field and (b) with the application of magnetic field for 2 min.

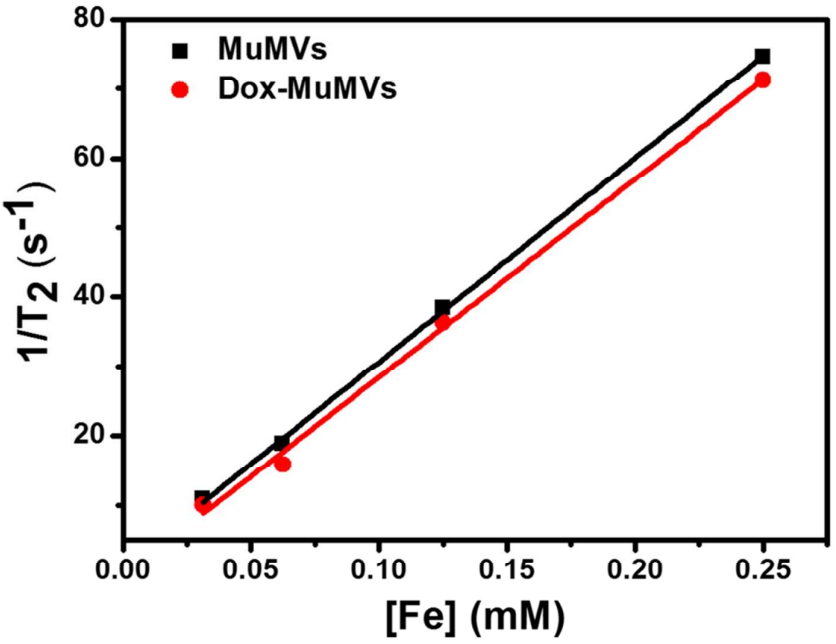

Figure S19. Spin-spin $1/T_2$ relaxation rates of MuMVs before (black) and after (red) Dox loading as a function of iron concentration.

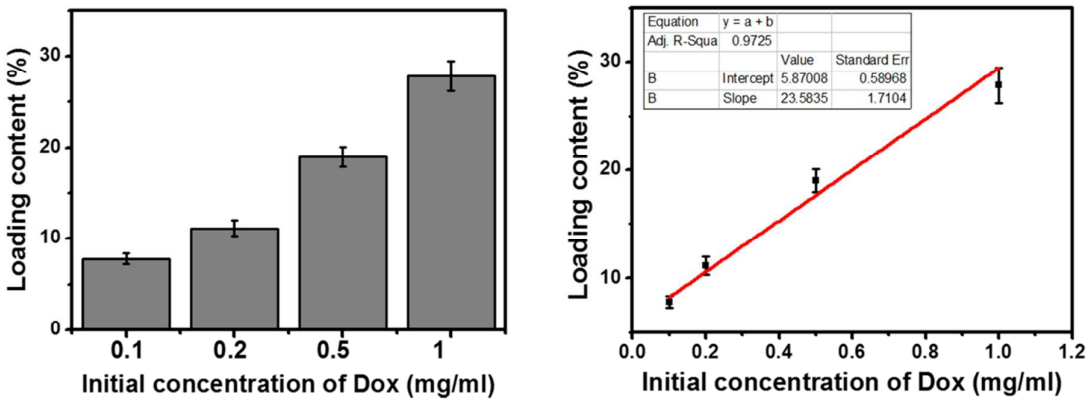

Figure S20. Loading content of Dox in MuMVs as a function of the initial concentrations of Dox.

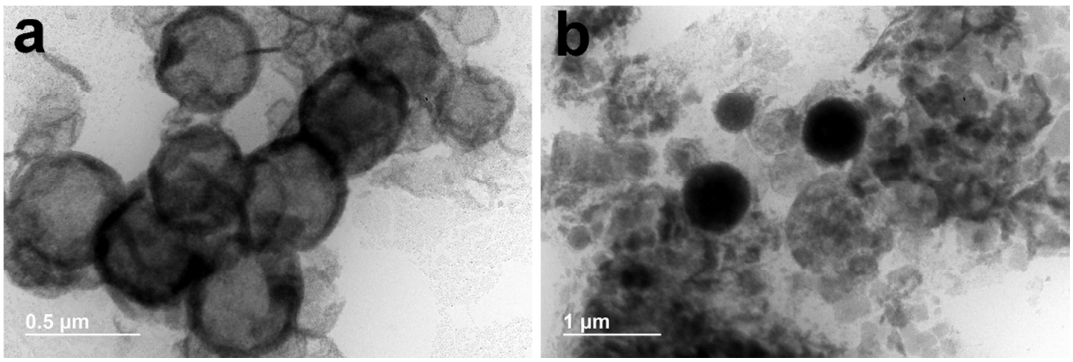

Figure S21. Assemblies of BCP-SPIONs by film rehydration of building blocks in Dox solutions with (a) 1.5 mg ml^{-1} and (b) 2.0 mg ml^{-1} of Dox.

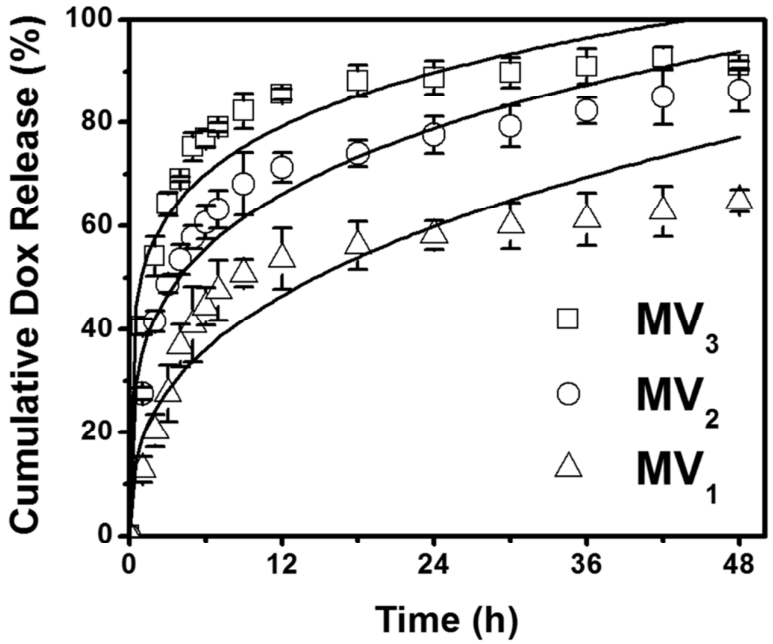

Figure S22. Controlled release of Dox from magnetic vesicles with different membrane thickness fitting the linear form of the empirical Korsmeyer-Peppas equation. The formation conditions of MVs are: MV_1 (DoMVs, W_{BCP}=0.8), MV_2 (MuMVs, W_{BCP}=1.6), and MV_3 (MuMVs, W_{BCP}=3.2).

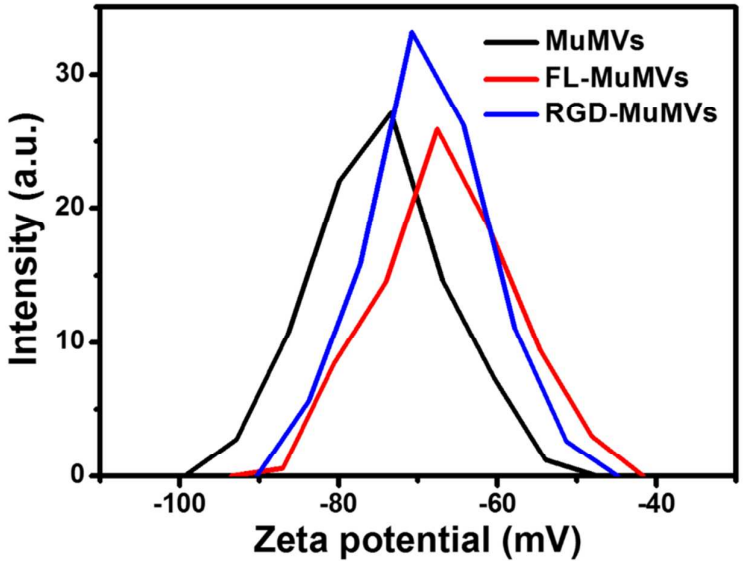

Figure S23. Reduced negative charge of MuMVs after conjugation with fluoresceinamine and RGD peptide.

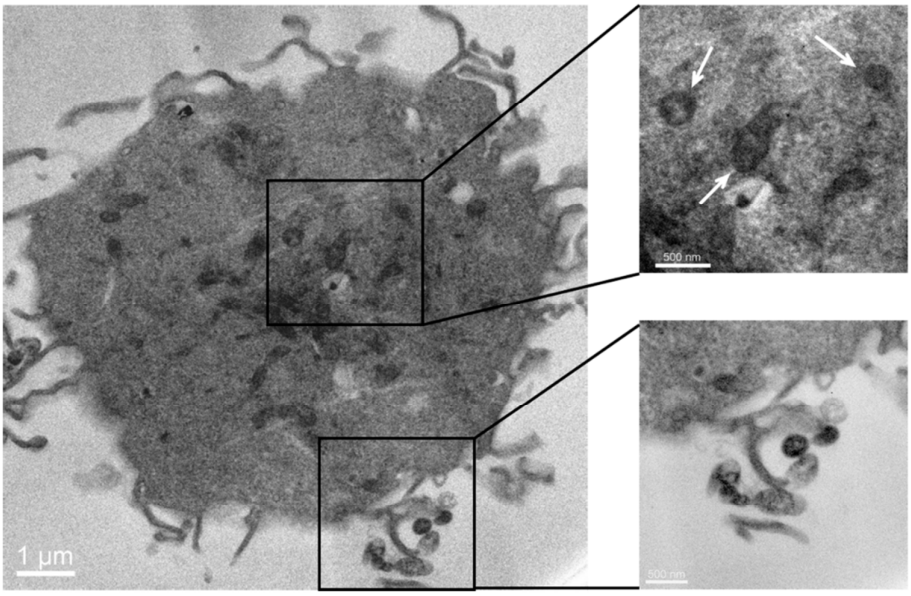

Figure S24. TEM images taken on U87MG cells incubated with MuMVs for 1 h. White arrows denote the vesicles inside the cell.

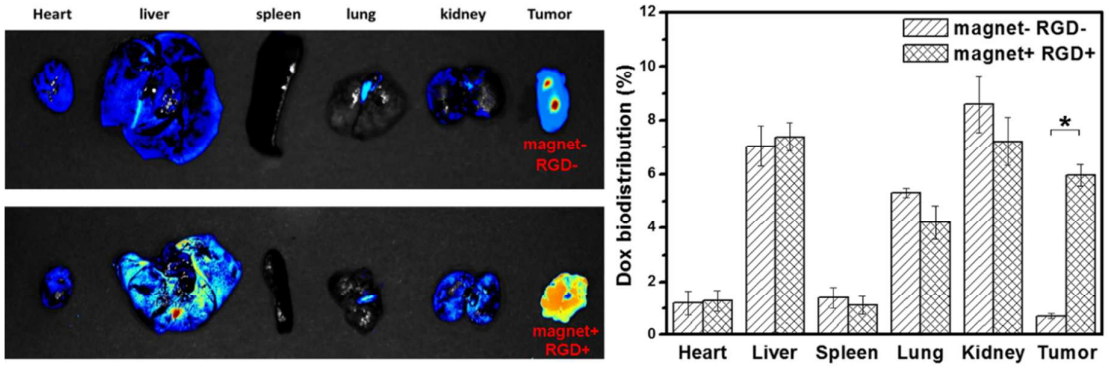

Figure S25. Biodistribution of Dox after intravenous injection of Dox-MuMVs (magnet-) and RGD-Dox-MuMVs (magnet+) into subcutaneous U87MG tumor-bearing mice. *, $p<0.01$.

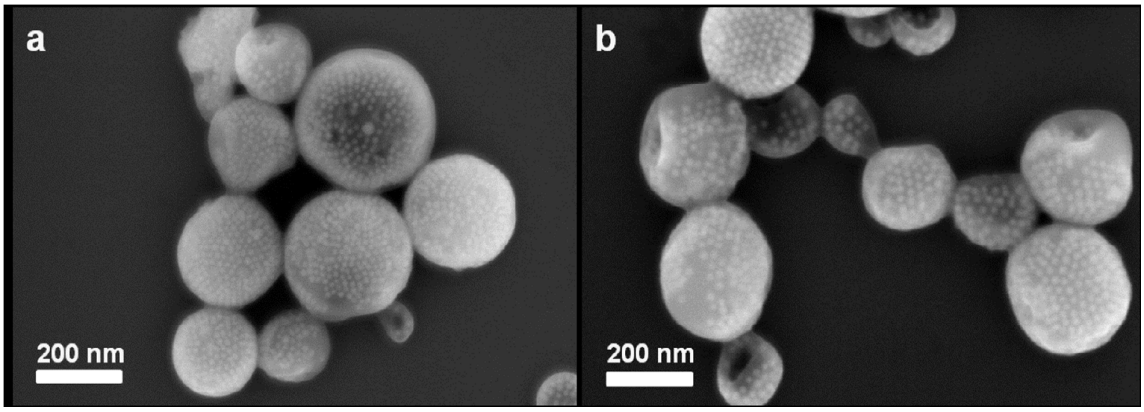

Figure S26. SEM images of MuMVs (a) before and (b) after filtration through a 200 nm filter.

References

[1] M. Mazur, A. Barras, V. Kuncser, A. Galatanu, V. Zaitzev, K. V. Turcheniuk, P. Woisel, J. Lyskawa, W. Laure, A. Siriwardena, R. Boukherroub, S. Szunerits, *Nanoscale* **2013**, *5*, 2692-2702.